

Identifying Compton-thick AGNs in the COSMOS

II. Among mid-infrared selected AGNs

Xiaotong Guo (郭晓通)^{1,2,4}, Qiusheng Gu (顾秋生)^{3,4,*}, Guanwen Fang (方官文)^{1,2}, Shiyong Lu (陆诗莹)^{1,2,4}, Fen Lyu (吕芬)^{1,2}, Yongyun Chen (陈永云)⁵, Nan Ding (丁楠)⁶, Mengfei Zhang (张孟飞)^{1,2}, Xiaoling Yu (俞效龄)⁵, and Hongtao Wang (王洪涛)⁷

¹ School of Physics and Astronomy, Anqing Normal University, Anqing 246133, China

² Institute of Astronomy and Astrophysics, Anqing Normal University, Anqing 246133, China
e-mail: guoxiaotong@aqnu.edu.cn

³ School of Astronomy and Space Science, Nanjing University, Nanjing, Jiangsu 210093, China
e-mail: qsgu@nju.edu.cn

⁴ Key Laboratory of Modern Astronomy and Astrophysics (Nanjing University), Ministry of Education, Nanjing 210093, China

⁵ College of Physics and Electronic Engineering, Qujing Normal University, Qujing 655011, China

⁶ School of Physical Science and Technology, Kunming University, Kunming 650214, China

⁷ School of Science, Langfang Normal University, Langfang 065000, China

Received September 30, 20XX

ABSTRACT

Context. Compton-thick active galactic nuclei (CT-AGNs), defined by column density $N_{\text{H}} \geq 1.5 \times 10^{24} \text{ cm}^{-2}$, are so heavily absorbed that their X-ray emission is often feeble, even undetectable by X-ray instruments. Nevertheless, their radiation is expected to be a substantial contributor to the cosmic X-ray background (CXB), predicting that CT-AGNs should comprise at least $\sim 30\%$ of the total AGN population.

Aims. In the Cosmological Evolution Survey (COSMOS), the identified CT-AGN fraction falls far below theoretical expectations, indicating that a substantial population of CT-AGNs is hidden due to their low photon counts or their flux below the current flux limits of X-ray instruments. This work focuses on identifying CT-AGNs hidden in mid-infrared (MIR)-selected AGNs.

Methods. First, we selected a sample of 1,104 MIR-selected AGNs that were covered but individually undetected by X-ray. Next, we reduced the X-ray data in the COSMOS and analyzed multiwavelength data in our sample to derive the key physical parameters required for CT-AGN identification.

Results. Using MIR diagnostics, we first find out 7 to 23 CT-AGN candidates. Their subsequent X-ray stacking analysis reveals a clear detection at $> 3\sigma$ significance in the soft band and only $> 1\sigma$ significance in the hard band. We fit the stacked soft- and hard-band fluxes with a physical model and confirm that these sources are absorbed by Compton-thick material. However, CT-AGNs constitute only 2.1% (23/1104) of our sample, significantly below the fraction predicted by CXB synthesis models, indicating that a considerable population of CT-AGNs remains missed by our selection. A comparison of host-galaxy properties between CT-AGNs and non-CT-AGNs reveals no significant differences.

Key words. Galaxies: active – Galaxies: nuclei – Infrared: galaxies – X-rays: diffuse background

1. Introduction

Active galactic nuclei (AGNs) are defined as galaxies hosting supermassive black holes (SMBHs, 10^6 – $10^9 M_{\odot}$) that have an Eddington ratio¹ exceeding the limit of 10^{-5} (Netzer 2015). These systems are powered by the accretion of surrounding matter through the SMBHs, thereby releasing their gravitational potential energy. Their emissions cover the entire electromag-

netic spectrum, exhibiting distinct radiation characteristics at varying distances from the central SMBHs. The AGN unification model suggests that the radiation across different bands originates from their specific substructures (Antonucci 1993; Urry & Padovani 1995; Netzer 2015). For instance, the accretion disk near the SMBH is heated by the viscous dissipation of gravitational potential energy during mass accretion, producing a broad ultraviolet (UV)-to-optical continuum spectrum (e.g., Richstone & Schmidt 1980). The hot corona, hovering above the accretion disk, generates luminous X-ray emission through inverse Compton up-scattering of UV-optical photons originating from the accretion disk (Liang 1979; Haardt & Maraschi 1991). The dusty torus, situated outside the corona and accretion disk, absorbs the intense radiation from the central engine and reprocesses it into thermal emission at longer mid-infrared (MIR) band (e.g., Antonucci 1993). Owing to the evolutionary stages of AGNs and the viewing angle effects, the majority of AGNs are obscured by large amounts of dust and gas

* qsgu@nju.edu.cn

¹ The Eddington ratio is defined as the ratio of the bolometric luminosity of the AGN to the Eddington luminosity, which represents the balance between the gravitational force and the radiation pressure. For a supermassive black hole with mass M_{BH} , the Eddington luminosity can be approximated as:

$$L_{\text{Edd}} = 1.5 \times 10^{38} \frac{M_{\text{BH}}}{M_{\odot}} \text{ erg s}^{-1}.$$

(e.g., [Hickox & Alexander 2018](#)). The high penetration ability of X-ray radiation, combined with the bright X-ray emissions from AGNs, makes X-rays an essential tool for distinguishing AGNs from other extragalactic sources and for investigating the obscured material within AGNs (e.g., [Xue 2017](#)). The neutral hydrogen column density (N_{H}) is a key parameter for describing the obscured AGNs in the X-ray band. The obscured AGNs exhibiting a column density of $N_{\text{H}} \geq 1.5 \times 10^{24} \text{ cm}^{-2}$ are classified as Compton-thick AGNs (CT-AGNs; e.g., [Comastri 2004](#)).

The cosmic X-ray background (CXB) is the radiation from the superposition of all discrete X-ray point sources, of which AGNs account for the vast majority ([Mushotzky et al. 2000](#); [Moretti et al. 2003](#); [Luo et al. 2017](#)). The most prominent observational feature of the CXB spectrum is a pronounced hump, marking the peak of its energy density, around 30 keV ([Revnivtsev et al. 2003](#); [Churazov et al. 2007](#); [Frontera et al. 2007](#); [Ajello et al. 2008](#)). Over the past several decades, theoretical modeling of the CXB spectrum has repeatedly demonstrated that only AGN population synthesis models incorporating a substantial fraction of CT-AGNs can successfully reproduce the complete spectral shape of the CXB (e.g., [Gilli et al. 2007](#); [Treister et al. 2009](#); [Burlon et al. 2011](#); [Akylas et al. 2012](#); [Ueda et al. 2014](#); [Ananna et al. 2019](#); [Georgantopoulos et al. 2025](#)). To date, the fraction of CT-AGNs remains uncertain and is a subject of hot debate. At low redshifts, such as in the local Universe, AGN population synthesis models predict that CT-AGNs account for 20–30% of the total AGN population detected by hard X-ray surveys such as Swift-BAT ([Burlon et al. 2011](#); [Ueda et al. 2014](#); [Ricci et al. 2015](#)). The denser atomic and molecular gas content in high-redshift galaxies (e.g., [Carilli & Walter 2013](#)), relative to the local Universe, increases the likelihood that AGNs hosted in these environments are heavily obscured, thereby leading to a higher expected fraction of CT-AGNs. For instance, [Buchner et al. \(2015\)](#) estimated that CT-AGNs account for $38^{+8}_{-7}\%$ of the total AGN population in X-ray deep-field surveys, while [Ananna et al. \(2019\)](#) found that this fraction increases to $56\% \pm 7\%$ for AGNs within the redshifts $z \approx 1$.

To observationally recover the intrinsic fraction of CT-AGNs in the total AGN population, it is essential to select an AGN sample that is unbiased against CT-AGNs. AGN samples selected through MIR methods meet this criterion due to the lower extinction at this waveband (e.g., [Li & Draine 2001](#)). Some studies have estimated that the fraction of CT-AGNs in MIR-selected AGN samples aligns with the theoretical predictions for the CXB (e.g., [Carroll et al. 2023](#); [Akylas et al. 2024](#); [Lyu et al. 2024](#)). Recently, [Annur et al. \(2025\)](#) directly measured a CT-AGN fraction of $32^{+30}_{-18}\%$ in a MIR-selected AGN sample within 15 Mpc, where the column densities are derived from broad-band X-ray spectral analysis. Similarly, [Boorman et al. \(2025\)](#) directly measured the CT-AGN fraction of $35\% \pm 9\%$ in a sample of 122 nearby ($z < 0.044$) AGNs primarily selected for their MIR colors. These results have already provided compelling evidence to support the AGN synthesis models of the CXB.

Nevertheless, attaining the theoretically anticipated fraction of CT-AGNs within X-ray surveys remains a significant challenge. The X-ray radiation of CT-AGNs is typically extremely faint, so their photon counts are low, even undetectable. These characteristics make CT-AGNs the most difficult population to detect in X-ray surveys (e.g., [Matt et al. 2000](#); [Comastri et al. 2015](#); [Padovani et al. 2017](#)). In particular, for sources with column densities $N_{\text{H}} \geq 10^{25} \text{ cm}^{-2}$, even in the local Universe, X-ray flux-limited surveys are biased against detecting CT-AGNs (e.g., [Ricci et al. 2015](#); [Koss et al. 2016](#); [Annur et al. 2025](#);

[Boorman et al. 2025](#)). X-ray surveys typically report an observed fraction of CT-AGNs below 15% (e.g., [Ricci et al. 2017b](#); [Masini et al. 2018](#); [Georgantopoulos & Akylas 2019](#)), which is significantly lower than theoretical model predictions, meaning that a large number of CT-AGNs remain unidentified or undiscovered. These missing CT-AGNs may still be hidden in AGNs that exhibit low photon counts (e.g., [Lambrides et al. 2020](#)) or that have not been detected by X-ray surveys (e.g., [Carroll et al. 2021](#)). To identify the missing CT-AGNs in the local Universe, the X-ray astronomy group at Clemson University and the extragalactic astronomy group at the INAF-OAS Bologna and INAF-IASF Palermo initiated a targeted project in 2017 to actively search for CT-AGNs, known as the Clemson-INAf CT-AGN Project ([Marchesi et al. 2018](#)). The project used a volume-limited sample of CT-AGNs with NuSTAR spectra, achieving a CT-AGN fraction of $20\% \pm 5\%$ within the redshift $z < 0.01$ ([Torres-Albà et al. 2021](#)). Similarly, a series of studies have focused on searching for the missing CT-AGNs in X-ray deep-field surveys. For example, [Guo et al. \(2021\)](#) identified eight missing CT-AGNs by using the multiwavelength techniques in the Chandra Deep Field-South (CDFs) survey. [Zhang et al. \(2025\)](#) used machine learning algorithms to identify 67 missing CT-AGNs, thereby raising the fraction of CT-AGNs to 20% in the CDFS survey. Numerous efforts have been made to search for the missing CT-AGNs in X-ray surveys, yet the theoretical expectations remain unmet.

The Cosmic Evolution Survey (COSMOS; e.g., [Scoville et al. 2007](#)) is a deep, multiwavelength survey covering a relatively large area of 2 deg^2 , aimed at measuring the evolution of galaxies and AGNs. The X-ray observations of this field are also crucial for resolving the CXB (e.g., [Buchner et al. 2015](#)). The Chandra X-ray telescope has covered the entire COSMOS, achieving a relatively deep average exposure (e.g., [Civano et al. 2016](#); [Marchesi et al. 2016](#)). However, the observed fraction of CT-AGNs in the COSMOS is significantly lower than theoretical expectations. For example, [Lanzuisi et al. \(2018\)](#) successfully identified 67 CT-AGNs from a sample of 1855 AGNs with high (>30) photon counts through X-ray spectral fitting. To find out the hidden CT-AGNs in the COSMOS, it is essential to establish and execute a series of specific tasks. [Guo et al. \(2025\)](#) have completed the first task and successfully identified 18 CT-AGNs. In this work, we aim to execute and complete the second task, focusing on identifying CT-AGNs among MIR-selected AGNs. This paper is structured as follows. Sect. 2 presents the data used to select AGNs via MIR colors and details the construction of our final sample. In Sect. 3, we describe the Chandra observations covering COSMOS and their data reduction. Sect. 4 presents the multiwavelength photometric data for the sample and the corresponding analysis. Sect. 5 presents our CT-AGN diagnostics, briefly discusses the missing CT-AGNs in our sample and the properties of CT-AGN host galaxies. A brief summary is presented in Sect. 6. We adopt a concordance flat Λ -cosmology with $H_0 = 67.4 \text{ km s}^{-1} \text{ Mpc}^{-1}$, $\Omega_{\text{m}} = 0.315$, and $\Omega_{\Lambda} = 0.685$ ([Planck Collaboration et al. 2020](#)). All quoted uncertainties correspond to the 1σ (68%) confidence level unless stated otherwise, while upper limits are given at the 3σ level.

2. The MIR-selected AGN Sample

2.1. MIR data Collation

To construct a high-quality MIR-selected AGN sample, we first systematically collated the MIR data. The primary data

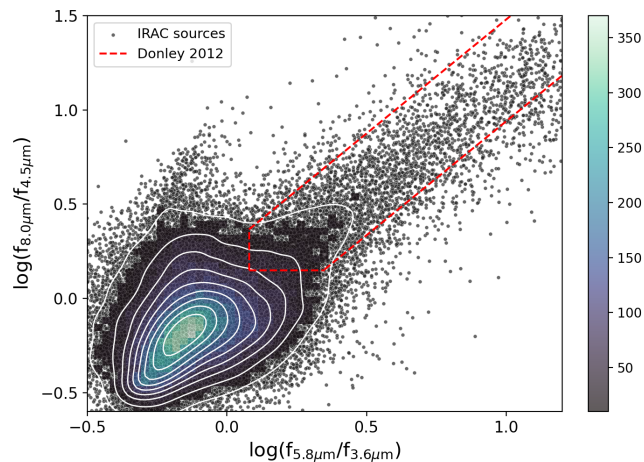


Fig. 1: IRAC color-color diagram of the MIR sources. The small gray dots represent all IRAC sources selected in the COSMOS. The region bounded by red dashed lines marks the MIR-AGN selection region of Donley et al. (2012). The sources within this region are classified as MIR-selected AGNs. The color bar and overlaid contours trace the number density gradient across the diagram.

source was the COSMOS2020 FARMER catalog (Weaver et al. 2022), which provides *Spitzer*/IRAC four-band (3.6 μm , 4.5 μm , 5.8 μm , 8.0 μm) photometric data. To meet the requirements for MIR AGN selection, the following constraints were applied to the MIR photometric data:

- (1). Sources with redshifts between 0.1 and 2 were selected.
- (2). Sources with IRAC magnitudes not less than the 3σ detection limit were chosen to ensure data reliability.
- (3). The flux-to-error ratio in each band was required to be greater than 5 to ensure high signal-to-noise ratios.

In the COSMOS2020 FARMER catalog, a total of 56,831 sources satisfy the above constraints. We have collected the four band flux densities of *Spitzer*/IRAC for use in the next section.

2.2. Selection of AGN sample

The unique colors of AGNs in the MIR band, especially between 3–5 μm , make their spectra appear redder than those of normal galaxies. Therefore, many studies use this feature to distinguish AGN from normal galaxies and identify them (e.g., Lacy et al. 2004, 2007, 2013; Donley et al. 2012; Assef et al. 2013; Chang et al. 2017). For example, the IRAC color-color diagrams most commonly used for AGN selection were defined by Lacy et al. (2004, 2007, 2013) and Donley et al. (2012). In this work, we adopted the AGN selection criterion of Donley et al. (2012), which is more stringent than others and yields a highly pure and reliable AGN sample. Fig. 1 presents an IRAC color-color diagram, plotting $\log(f_{5.8\mu\text{m}}/f_{3.6\mu\text{m}})$ against $\log(f_{8.0\mu\text{m}}/f_{4.5\mu\text{m}})$. The sources within the red dashed lines are AGNs selected using the criteria from Donley et al. (2012), totaling 1,545. Among them 252 are X-ray sources, of which nine have been classified as CT-AGNs by Lanzuisi et al. (2018) and Guo et al. (2025).

To identify CT-AGNs among AGNs undetected by X-ray in the COSMOS, we applied the following constraints to the MIR-selected AGN sample:

- (1). Remove known X-ray sources from the MIR-selected AGNs.
- (2). Eliminate sources lacking X-ray observations (i.e., those with exposure time = 0).
- (3). To avoid overestimating the flux upper limits (see Sect. 3.3) of MIR-selected AGNs due to nearby bright X-ray sources, we exclude any sources located within $6''$ of known X-ray sources.

After this screening, our final AGN sample comprises 1,104 sources. Cols. 1–3 of Table A.1 list their IDs, RA, and DEC. The photometric redshifts of our AGN sample are taken from the COSMOS2020 FARMER catalog, measured by LePhare using the galaxy templates. For the bright sources, Weaver et al. (2022) find a normalized median absolute deviation of only 0.009 in their photometric redshifts; even in the faintest bin (25 mag < i < 27 mag) the normalized median absolute deviation is 0.036. Col. 4 of Table A.1 lists their photometric redshifts.

3. X-ray Observations and Data Reduction

3.1. Overview of Chandra's Observations in COSMOS

To identify (or probe) AGNs with varying redshifts in the COSMOS and investigate black hole accretion history as well as the co-evolution of AGNs with their host galaxies, Elvis et al. (2009) conducted *Chandra* observations during 2006–2007, accumulating a total exposure of 1.8 Ms. These observations covered the central 0.5 deg² with an effective exposure of approximately 160 ks and an outer 0.4 deg² area with an effective exposure of approximately 80 ks. Subsequently, Civano et al. (2016) added further *Chandra* observations during 2013–2014, increasing the total exposure to 2.8 Ms. These additional observations covered the remaining area (the outer 0.4 deg² from Elvis et al. 2009) with an effective exposure of approximately 80 ks and increased the effective exposure over the central 1.5 deg² to approximately 160 ks. As a result, the combined observations totaling approximately 4.6 Ms covered a region of 2.2 deg² in the COSMOS. For detailed information on observation files, including observation and exposure times.

3.2. Data acquisition and reduction

To determine the X-ray flux upper limits for each AGN in our sample, their exposure times and counts are required. As the exposure and image maps are not archived, we first retrieved all 117 raw event files covering the COSMOS from the *Chandra* X-ray Center². Next, we processed these 117 raw event files through the following detailed steps to extract the required exposure times and counts.

We processed the data reduction using CIAO 4.17 software tools (Fruscione et al. 2006) and CALDB 4.12.0. We used the *chandra_repro* script to reprocess the data, automating the CIAO recommended steps and generating new level 2 event files. Subsequently, we removed ACIS-I Background Flares using the *dmcopy* and *dmextract* scripts, following the standard Science Threads from the *Chandra* X-ray Observatory. Finally, all 117 observations were merged with the *merge_obs* script to produce exposure-corrected images and the corresponding modeled background maps.

² <https://cda.harvard.edu/chaser/>

3.3. X-ray luminosity upper limit estimations

Our MIR-selected AGNs are individually undetected in X-rays, their X-ray luminosities cannot be measured directly. Consequently, we quote only upper limits, calculated with the equation (Alexander et al. 2003),

$$L_{2-10}^{\text{up-limit}} = 4\pi \cdot D_L^2 \cdot f_{2-10}^{\text{up-limit}} \cdot (1+z)^{\Gamma-2},$$

where D_L is the luminosity distance, $f_{2-10}^{\text{up-limit}}$ represents the upper limit of the flux in the 2–10 keV within the observed frame, z is the redshift, and Γ is the photon index used for k-corrections, which is fixed to the value of 1.4 (Civano et al. 2016). The upper limit of the X-ray flux density is calculated by

$$f_{2-10}^{\text{up-limit}} = R_{\text{lim}} \times (\text{CF} \times 10^{-11}) \text{ erg} \cdot \text{s}^{-1},$$

where R_{lim} is the upper limit of the count rate at the undetected source and CF is the energy conversion factor, set at 3.06 (Civano et al. 2016). The upper limit of the count rate for undetected sources is calculated by

$$R_{\text{lim}} = \frac{B_{3''}^{3\sigma}}{T_{\text{exp}}},$$

where T_{exp} represents the effective exposure time at the source location, $B_{3''}^{3\sigma}$ denotes the 3σ upper limit on the background counts measured within a $3''$ -radius aperture centered on the source. The 3σ upper limit on the background counts is calculated using Equation 9 of Gehrels (1986), giving

$$B_{3''}^{3\sigma} \approx (B_{3''} + 1) \left[1 - \frac{1}{9(B_{3''} + 1)} + \frac{3}{3\sqrt{B_{3''} + 1}} \right]^3,$$

where $B_{3''}$ represents the 0.5–8 keV background counts measured within a $3''$ -radius aperture centered on the source, after correction for the energy-encircled fraction. The background counts for AGNs are determined by summing all values from a $3''$ radius circle centered at their respective coordinates in the modeled background map. Similarly, the exposure times for the AGNs are determined by reading the values from the exposure map at their respective coordinates. Fig. 2 shows the coordinates of MIR-selected AGNs on the exposure map and their corresponding exposure times. Cols. 5–6 of Table A.1 give the $3''$ aperture background counts $B_{3''}$ and exposure time T_{exp} for each source.

Applying the calculation process described above, we derived X-ray luminosity upper limits for the entire MIR-selected AGN sample. Cols. 7–8 of Table A.1 list the upper limits of flux density and luminosity in the 2–10 keV band.

4. Analysis of multiwavelength data

4.1. Multiwavelength photometric data

Identifying CT-AGNs among MIR-selected AGNs requires ascertaining the MIR radiation from AGNs. Thus, we need to construct the spectral energy distributions (SEDs) for these sources to decompose the AGN's contribution to the MIR emission. This process requires multiwavelength photometric data.

The multiwavelength photometric data used in this work span the far-UV (FUV, 1526 Å) to the far-infrared (FIR, 500 μm). Among them, the photometric data covering the wavelength range from the FUV to the MIR (27 bands in total) are sourced from the COSMOS2020 FARMER catalog

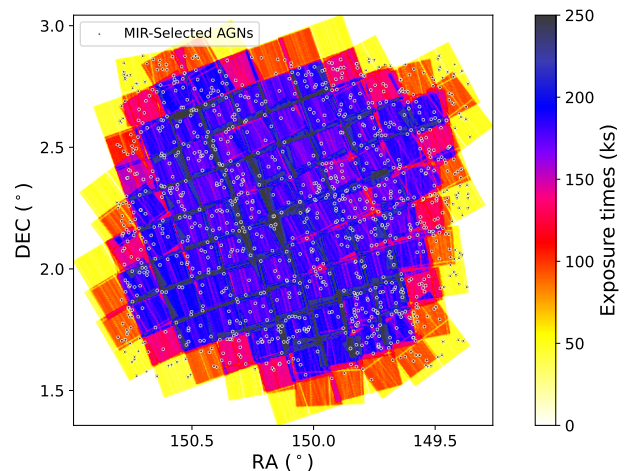


Fig. 2: Merged Chandra exposure map of the COSMOS, overlaid with the positions of MIR-selected AGNs (black dots) used in this work. The color bar indicates the effective exposure time for the corresponding X-ray coverage.

(Weaver et al. 2022). These bands include the GALEX FUV and NUV band, MegaCam U band, CFHT U band, five Subaru HSC bands (g, r, i, z, and y), 12 Subaru Suprime-Cam medium bands (IB427, IB464, IA484, IB505, IA527, IB574, IA624, IA679, IB709, IA738, IA767, and IB827), four VISTA VIRCAM broad bands (Y, J, H, and K_s), and four Spitzer IRAC bands (ch1, ch2, ch3, and ch4). Moreover, the FIR photometric data are sourced from the COSMOS2015 catalog (Laigle et al. 2016), including MIPS 24 μm, PACS 100 μm, PACS 160 μm, SPIRE 250 μm, SPIRE 350 μm, and SPIRE 500 μm. Where photometric data in a given band are missing, we use the corresponding flux upper limits in the SED analysis.

4.2. Analysis of SEDs

The SED analysis of AGNs is a widely used technique that not only provides detailed information about AGNs but also reveals the properties of their host galaxies (e.g., Guo et al. 2020), such as AGN luminosity, rest-frame 6 μm luminosity for the AGN, stellar mass (M_*), and the star formation rate (SFR). In this work, we use *Code Investigating GALaxy Emission* (CIGALE; V2022.1; Boquien et al. 2019), an open Python code containing the template of galaxies and AGNs, to conduct the analysis of AGNs in our sample and obtain the required parameters.

Since all sources in our sample are MIR-selected AGNs, we have used templates that incorporate both the galaxy and AGN characteristics to achieve the most accurate SED fitting. The galaxy templates in CIGALE are generated by integrating four distinct modules, including the star formation history (SFH), the single stellar population (SSP) model (Bruzual & Charlot 2003), the dust attenuation (DA; Calzetti et al. 2000), and the dust emission (DE; Draine & Li 2007; Dale et al. 2014). The AGN component in our analysis is a module developed by Fritz et al. (2006). The modules and parameters used for SED fitting are summarized in Table 1. Additionally, for sources using upper flux limits in certain bands, the *lim_flag* is set to "noscaling". Given the vast parameter space, quickly constructing a model on the computer is not feasible. Thus, we adopted an iterative methodology to expedite the acquisition of the best-fitting SEDs.

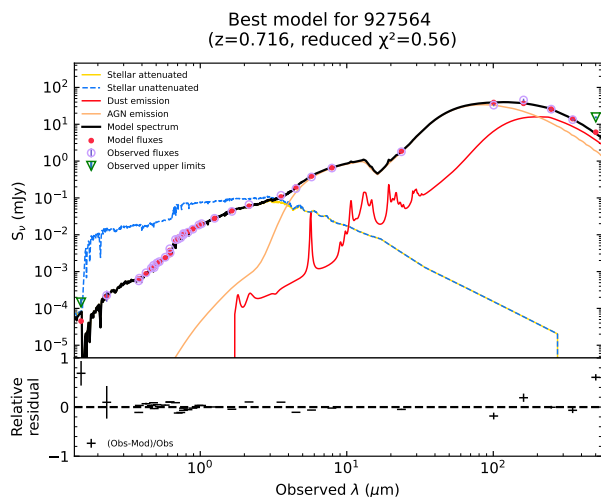


Fig. 3: Example of best-fitting SED for an AGN. The solid black line indicates the best-fitting model. The dashed blue, solid gold, and solid red lines represent unattenuated stellar, attenuated stellar, and dust emission, respectively. The solid apricot line indicates AGN emission. The strawberry filled circles, pastel-purple open circles, and green open inverted triangles denote model predictions, observed fluxes, and observed upper limits, respectively. The lower panel indicates the residual of the best fitting.

Fig. 3 shows the best-fitting SED for an AGN. To assess the reliability of the fitted AGN components, we refit SEDs using only the galaxy templates. A markedly better fit (indicated by a lower χ^2) with the combined galaxy+AGN templates than with the galaxy-only templates implies that the fitted AGN components can indeed represent the contribution of the actual AGNs in their SEDs. We used the Bayesian information criterion (BIC) to quantify the significance or confidence of the AGN components (see Appendix C of Guo et al. 2025, for details).

Through SED fitting, we obtained the best-fitting SED for each source and derived the corresponding physical parameters. Cols. 9–10 of Table A.1 are rest-frame $6\ \mu\text{m}$ luminosity for the AGN and the AGN components’ confidence. Col. 11 of Table A.1 presents M_\star , the derived outcome of SED fitting. However, since the SFR derived from SED fitting relies on the chosen SFH model (Gao et al. 2019), we instead use the calibration method proposed by Bell et al. (2005) to estimate the SFR using UV and IR luminosities. This calibration is scaled to the Chabrier (2003) initial mass function for accuracy. Specifically, the SFR is calculated using the formula

$$\text{SFR}(M_\odot \text{ yr}^{-1}) = 1.09 \times 10^{-9} (2.2L_{\text{UV}} + L_{\text{IR}}), \quad (1)$$

where $L_{\text{UV}} = \nu L_\nu$ is an estimation of the integrated 1216 – 3000 Å rest-frame UV luminosity, and L_{IR} is the 8 – 1000 μm rest-frame IR luminosity. Both L_{UV} and L_{IR} are in units of L_\odot . Col. 12 of Table A.1 lists the SFR of each source.

5. Diagnostic CT-AGNs and Discussion

5.1. MIR diagnostics

The emissions from the corona and dust torus of AGNs are considered good tracers of the accretion disk’s emission. Consequently, a strong correlation is expected between X-ray and MIR emissions in AGNs. Several studies have investigated this relationship in radio-quiet AGNs (e.g.,

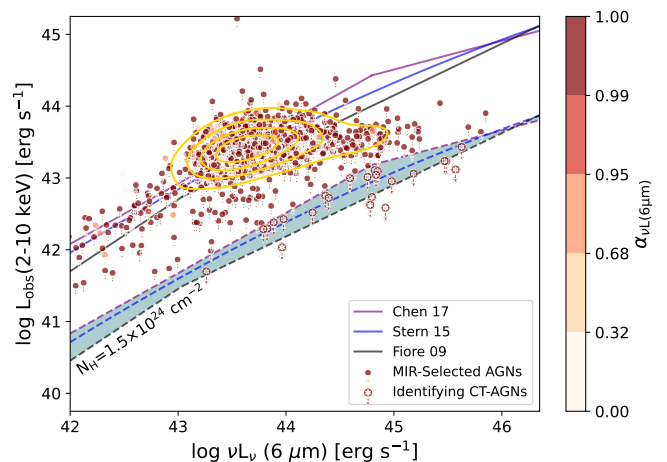


Fig. 4: Observed X-ray luminosity in the rest-frame 2–10 keV band as a function of the $6\ \mu\text{m}$ luminosity for fit AGN component. The solid purple, blue, and black lines represent the relation for Chen et al. (2017), Stern (2015), and Fiore et al. (2009), respectively. The dashed lines indicate the same relationships but where the X-ray luminosities are absorbed by a column density of $N_{\text{H}} = 1.5 \times 10^{24}\ \text{cm}^{-2}$. The circles are MIR-selected AGNs with a fit AGN component. The color bar represents the confidence coefficient of the $6\ \mu\text{m}$ luminosity for a fit AGN component (or the fit AGN components). The cutting stars within the large circles represent CT-AGNs identified using the relationship between MIR and X-ray luminosities.

Fiore et al. 2009; Mateos et al. 2015; Stern 2015; Chen et al. 2017; Esparza-Arredondo et al. 2019, 2021). Due to the low optical depth in the MIR band, the MIR radiation from CT-AGNs is not significantly suppressed. As the column density increases, the torus absorbs more nuclear X-ray emission and re-radiates it in the MIR, potentially boosting the MIR luminosity. However, this effect is extremely weak: the AGN X-ray luminosity is 1–2 dex below its UV–optical continuum (Steffen et al. 2006; Lusso et al. 2010), so even complete absorption and re-radiation in the MIR would contribute negligibly compared with the direct disk-dust heating. Ricci et al. (2017b) indeed found no significant increase in MIR luminosity with column density. Consequently, the intrinsic X-ray and MIR luminosities of AGNs are still expected to follow the above relations. However, because the X-ray radiation of CT-AGNs is heavily absorbed, their observed X-ray luminosities fall below the values predicted by these relations. Given that the AGNs in our sample are not detected in X-rays, we adopt the corresponding X-ray luminosity upper limits as their observed luminosities and use these relationships to identify CT-AGNs.

Fig. 4 shows the observed X-ray luminosity in the rest-frame 2–10 keV band as a function of the $6\ \mu\text{m}$ luminosity for the fit AGN component. The solid purple, blue, and black lines represent the relation for Chen et al. (2017), Stern (2015), and Fiore et al. (2009), respectively. Assuming the intrinsic 2–10 keV spectrum of each AGN is modeled in *Xspec* with *phabs*powerlaw+constant*powerlaw+pexmon* (see Appendix D of Guo et al. 2025 for details), the dashed lines represent the same relationships between MIR and X-ray luminosities after the X-ray spectra have been absorbed by gas with a column density of $N_{\text{H}} = 1.5 \times 10^{24}\ \text{cm}^{-2}$. This means that the sources within or below the shaded area in Fig. 4 should be clas-

Table 1: Module assumptions for SED fitting.

Component (1)	Module (2)	Parameter (3)	Value (4)
Galaxy	SFH (delayed)	tau_main (Myr)	20 – 8000 (in steps of 10)
		age_main (Myr)	200 – 13000 (in steps of 10)
	tau_burst (Myr)	10 – 200 (in steps of 1)	
	age_burst (Myr)	10 – 200 (in steps of 1)	
SSP (BC03)	imf	0, 0.0001, 0.0005, 0.001, 0.005, 0.01, 0.05, 0.1, 0.15, 0.20, 0.25, 0.3, 0.40, 0.50	
	metallicity	1 (Chabrier)	
DA (dustatt_calzleit)	E_BV_nebular (mag)	0.005, 0.01, 0.025, 0.05, 0.075, 0.10, 0.15, 0.20, 0.25, 0.30, 0.35, 0.40, 0.45, 0.50, 0.55, 0.60	
DE (dl2014)	qpah	1.12, 1.77, 2.50, 3.19	
	umin	5.0, 6.0, 7.0, 8.0, 10.0, 12.0, 15.0, 17.0, 20.0, 25.0	
	alpha	2.0, 2.1, 2.2, 2.3, 2.4, 2.5, 2.6, 2.7, 2.8	
	gamma	0.02	
AGN	AGN (Fritz2006)	r_ratio	10, 30, 60, 100, 150
		tau	0.1, 0.3, 0.6, 1.0, 2.0, 3.0
		beta	-1.00, -0.75, -0.50, -0.25, 0.00
		gamma	0.0, 2.0, 4.0, 6.0
		opening_angle	60, 100, 140
		psy	0.001, 10.1, 20.1, 30.1, 40.1, 50.1, 60.1, 70.1, 80.1, 89.99
		fracAGN	0.0, 0.05, 0.1, 0.15, 0.2, 0.25, 0.3, 0.35, 0.4, 0.45, 0.5, 0.55, 0.6, 0.65, 0.7, 0.75, 0.8, 0.85, 0.9, 0.95, 0.99

sified as CT-AGNs. Circles tipped with downward arrows denote the AGNs in our sample, their colors indicating the confidence levels of the fitted AGN components. As shown in Fig. 4, 23 AGNs fall within or below the shaded area, suggesting that they may be CT-AGNs. However, considering the variability in the relations provided by Chen et al. (2017) and Fiore et al. (2009), a range of possible CT-AGN candidates is 7 to 23. To further determine whether they are CT-AGNs, we must assess the reliability of their fitted AGN components. These sources, whose fitted AGN components exhibit a high confidence coefficient ($\alpha_{AGN} > 0.95$), support a CT-AGN classification, whereas those with a low confidence coefficient ($\alpha_{AGN} < 0.95$) cannot be reliably identified as CT-AGNs. Finally, a total of 23 AGNs located within or below the shaded region exhibit high confidence coefficients, supporting their diagnosis as CT-AGNs. These CT-AGNs are marked in Fig. 4 by cutting stars within the large circles. Col. 13 of Table A.1 also lists their classification, "1" represents CT-AGN identified in this work.

5.2. Stacking Analysis for CT-AGNs

In the preceding section, we successfully find out 7 to 23 CT-AGN candidates. Because these AGNs are individually undetected in X-rays, we cannot extract their X-ray spectra and determine their column densities. To confirm heavy absorption in the X-ray band, we perform X-ray stacking analysis on these 23 AGNs using the publicly available CSTACK V4.5 tool (Miyaji et al. 2008)³. This analysis adopts the default maximum off-axis angle, 3'' source aperture, 6'' background annulus, and automatic exclusion of known X-ray sources. The output of CSTACK includes the stacked photon count rates and their errors for both the soft (0.5–2 keV) and hard (2–8 keV) bands, along with the corresponding stacked images. Fig. 5 presents the stacking results: the stacked AGNs are clearly detected at $> 3\sigma$ significance in the soft band and marginally detected at $> 1\sigma$ in the hard band. The stacked photon count rates in

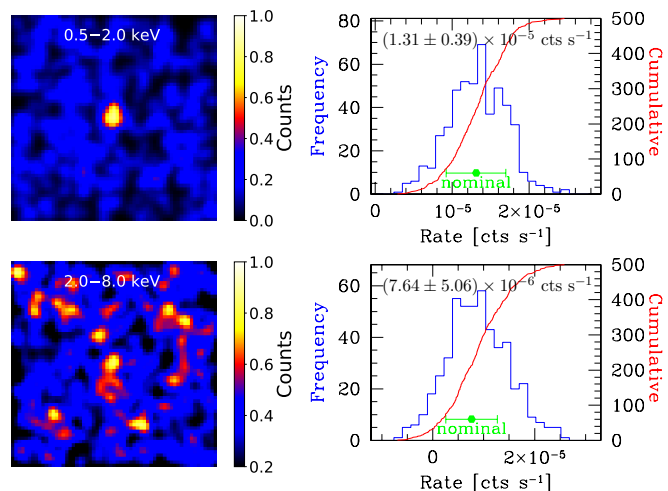


Fig. 5: X-ray stacking results for the 23 CT-AGNs identified by MIR diagnostics. Left: stacked images in the 0.5–2 keV (top) and 2–8 keV (bottom) bands. Right: corresponding bootstrap histograms of the net count rates; green lines indicate the mean count rates and 1σ confidence intervals. Detections exceed 3σ significance in soft band, while only exceed 1σ significance in hard band.

the soft and hard bands are $(1.31 \pm 0.39) \times 10^{-5}$ cts s^{-1} and $(7.64 \pm 5.06) \times 10^{-6}$ cts s^{-1} , respectively.

Assuming the AGN X-ray emission follows a simple power-law spectrum with photon flux density $F(E) \propto E^{-\Gamma}$, we convert the soft- and hard-band count rates into photon fluxes by adopting effective areas of 600 cm^2 and 350 cm^2 , and mean photon energies of 1.2 keV (soft) and 4.0 keV (hard). This derives a photon index $\Gamma = 0.0 \pm 0.6$. Assuming a Galactic absorption of $N_H = 2.6 \times 10^{20}$ cm^{-2} , we use a tool of PIMMS V4.15⁴ to estimate

³ CSTACK was developed by Takamitsu Miyaji and is available at <https://lambic.astrosen.unam.mx/cstack/>

⁴ <https://cxc.harvard.edu/toolkit/pimms.jsp>

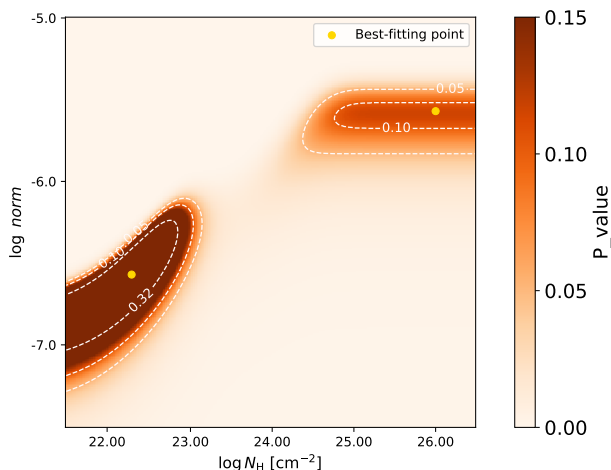


Fig. 6: The p-value distribution in the $\log N_{\text{H}}-\log \text{norm}$ plane. White contours mark $p = 0.05, 0.10$ and 0.32 ; the golden solid circle indicates the best-fit point.

soft- and hard-band fluxes of $(7.57 \pm 2.25) \times 10^{-17} \text{ erg cm}^{-2} \text{ s}^{-1}$ and $(2.34 \pm 1.55) \times 10^{-16} \text{ erg cm}^{-2} \text{ s}^{-1}$, respectively.

To further constrain the absorption of these sources, we fitted the soft- and hard-band fluxes in *Xspec* with the *zphabs*zpowerlw+constant*zpowerlw+pexmon* model. The redshift was fixed at the mean value of the 23 sources ($z = 0.92$), the photon index at 1.9, the inclination angle at 85° , and the scattered fraction at 0.005; only the column density N_{H} and normalisation *norm* were allowed to vary, while all remaining parameters were kept at their default values. Fig. 6 presents the p-value distribution in the $\log N_{\text{H}}-\log \text{norm}$ plane obtained by fitting the soft- and hard-band fluxes with our model. In $\log N_{\text{H}}-\log \text{norm}$ plane, the data are consistent with the model at the 95% confidence level within two distinct parameter regions, corresponding to Compton-thin and Compton-thick solutions, respectively. The golden solid circles mark the best-fitting points in both regions, with corresponding column densities of $2.09 \times 10^{22} \text{ cm}^{-2}$ and $9.55 \times 10^{25} \text{ cm}^{-2}$, respectively. The X-ray upper limits of these 23 sources already fall below the relationships between MIR and X-ray luminosities after absorbing by Compton-thick material. If their absorption were located in the Compton-thin region, the majority of them would have to be intrinsically X-ray weak AGNs. However, the intrinsic incidence of X-ray weak AGNs is far lower than that of CT-AGNs, making it extremely improbable that most of them are X-ray weak AGNs. The Compton-thin solution can therefore be ruled out. Within Compton-thick region, the 95% confidence level demands $\log N_{\text{H}} > 24.38$, while the 90% confidence level requires $\log N_{\text{H}} > 24.76$. Both thresholds lie well above the Compton-thick limit, providing direct and compelling evidence that these sources are CT-AGNs.

5.3. Missed Diagnosis of CT-AGNs

Although MIR-selected AGN samples are incomplete, numerous studies have shown that their CT-AGN fraction closely matches—or even reaches—the theoretical expectation of CXB (e.g., Lyu et al. 2024; Boorman et al. 2025; Annuar et al. 2025). Our MIR-selected sample excludes X-ray-detected AGNs, which preferentially select less absorbed AGNs. Consequently,

we expect the CT-AGN fraction in our MIR-selected sample to markedly exceed that predicted by CXB models. However, our MIR diagnostics identified only 23 CT-AGNs, 2.1% (23/1104) of the MIR-selected sample, significantly below the fraction expected from CXB synthesis models. This discrepancy clearly exceeds statistical error, indicating that MIR diagnostics miss a large number of CT-AGNs. Based on our analysis of the CT-AGN fraction within our sample, we infer that at least 300 CT-AGNs remain unidentified. With the current data and methods, we are still unable to find these missing CT-AGNs. To identify these missed CT-AGNs, the most direct and efficient approach is to conduct significantly deeper X-ray exposures of the COSMOS in the future. On the one hand, deeper exposures will enhance detection sensitivity, revealing AGNs that are currently buried in the background. This may not only confirm their existence but also allow column density measurements via X-ray spectral fitting, thereby reliably identifying CT-AGNs. On the other hand, for AGNs that remain undetected even after deep exposures, longer integrations will push their X-ray luminosity upper limits to lows, markedly enhancing the discriminatory power of MIR diagnostics.

5.4. The properties of CT-AGN host galaxies

CT-AGNs are widely regarded as an early, heavily obscured phase of AGN evolution (e.g., Guo et al. 2023). Their growth is intimately coupled to the host-galaxy environment, as evidenced by the tight $M_{\text{BH}}-\sigma_*$ relation (e.g., Ferrarese & Merritt 2000) and the role of AGN feedback in regulating star formation (e.g., Bower et al. 2006), which together support a coevolutionary scenario between AGNs and their host galaxies (e.g., Kormendy & Ho 2013). CT-AGNs are considered to preferentially host in galaxies with a significant amount of dense gas (Kocevski et al. 2015; Ricci et al. 2017a). Intense AGN radiation compresses their surrounding dense gas, potentially triggering star formation activity within their host galaxies. The host galaxies of CT-AGNs in the local universe exhibit a high level of star formation (e.g., Hopkins et al. 2006; Goulding et al. 2012). Zhang et al. (2025) find that the host galaxies of CT-AGNs in the CDFS exhibit higher levels of star formation activity than those of non-CT-AGNs. Andonie et al. (2022) suggest that obscured AGNs have star formation rates ≈ 3 times higher than unobscured systems in the COSMOS. However, Gilli et al. (2022) suggest that the host galaxies of high-redshift AGNs are different from those of AGNs in the local universe. Guo et al. (2025) report similar stellar mass and SFR distributions for CT-AGN and non-CT-AGN host galaxies; while their sample contains only 18 CT-AGNs, which is insufficient for statistically robust conclusions. Using a substantially larger sample, we will re-examine the SFRs and stellar masses of CT-AGN host galaxies relative to those of non-CT-AGNs.

Because a significant number of CT-AGNs in our sample remain unidentified, we cannot extract a pure non-CT-AGN sample. We therefore adopt the non-CT-AGNs provided by Guo et al. (2025) as the control sample, and combine their CT-AGNs with the 23 newly identified in this work to construct the final CT-AGN sample. Fig. 7 presents relationships, known as the main sequence, between SFRs and stellar masses of the host galaxies for both CT-AGNs and non-CT-AGNs. A Kolmogorov–Smirnov test (KS test) of stellar mass distributions for their host galaxies gives $p = 0.33$; repeating the KS test on their SFR distributions yields $p = 0.20$. Although these values are slightly lower than those reported by Guo et al. (2025), they still indicate no significant difference between the two distribu-

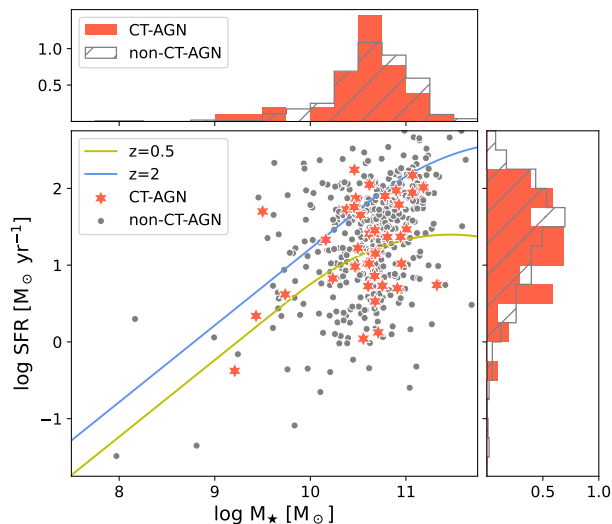


Fig. 7: The relationship of the main sequence in AGN host galaxies. The solid red stars indicate the CT-AGNs, and the gray circles represent non-CT-AGNs.

tions. Our findings, therefore, do not support a possible correlation between intense star formation and CT-AGNs reported by Zhang et al. (2025). This finding is likely due to the limited size of our CT-AGN sample, which is still too small for statistically robust conclusions. In future work, we will enlarge the CT-AGN sample and further study whether there are differences in the host galaxies of both CT-AGNs and non-CT-AGNs.

6. Summary

In this work, we aim to identify CT-AGNs hidden in AGNs whose X-ray flux is below the current flux limits in the COSMOS. First, we selected a sample of 1,104 MIR-selected AGNs that were covered but individually undetected by X-ray. Then, we reduced the Chandra observational data covering the field and derived upper limits on the X-ray luminosity for all AGNs in our sample. We subsequently collected multiwavelength photometric data for the sample and extracted key physical parameters for each source through SED fitting, such as $6\ \mu\text{m}$ luminosities of AGNs, stellar masses, and SFRs. After that, through MIR diagnosis, 7 to 23 sources could be identified as CT-AGNs. To confirm that our CT-AGNs are indeed heavily absorbed in the X-ray band, we performed a stacking analysis. The stacked signal is detected at 3σ significance in the soft band, with a flux of $(7.57 \pm 2.25) \times 10^{-17}\ \text{erg cm}^{-2}\ \text{s}^{-1}$, whereas the hard-band excess is only 1σ significant, corresponding to $(2.34 \pm 1.55) \times 10^{-16}\ \text{erg cm}^{-2}\ \text{s}^{-1}$. Fitting the stacked soft- and hard-band fluxes with the $zphabs*zpowerlw+constant*zpowerlw+pexmon$ model obtained two parameter regions that are consistent with the data at the 95% confidence level, corresponding to Compton-thin and Compton-thick solutions. The Compton-thin solution can be ruled out, leaving the Compton-thick absorber as the only viable scenario and confirming these sources as CT-AGNs. We fitted their soft- and hard-band fluxes with the $zphabs*zpowerlw+constant*zpowerlw+pexmon$ model, and found that when Compton-thick absorption was included did the

model provide a satisfactory fit to both bands. This provides direct and compelling evidence that these sources are CT-AGNs. Although we have already identified some CT-AGNs in the MIR-selected AGNs, a considerable population of CT-AGNs was still missed by our selection. Therefore, we estimated and discussed the number of missed CT-AGNs in our sample and proposed a practical strategy to search for them. Finally, comparing host-galaxy properties between CT-AGNs and non-CT-AGNs, we did not find evidence for a correlation between intense star formation and CT-AGNs.

Data availability

Table A.1 is only available in electronic form at the CDS via anonymous ftp to cdsarc.u-strasbg.fr (130.79.128.5) or via <http://cdsweb.u-strasbg.fr/cgi-bin/qcat?J/A+A/>.

Acknowledgements. We sincerely thank the anonymous referee for useful suggestions. We acknowledge the support of the *National Nature Science Foundation of China* (No. 12303017). This work is also supported by *Anhui Provincial Natural Science Foundation* project number 2308085QA33. QSGU is supported by the *National Nature Science Foundation of China* (Nos. 12192222, 12192220, and 12121003). L.S.Y. is supported by the *National Nature Science Foundation of China* (No. 12503011). F.L. is supported by the *National Nature Science Foundation of China* (No. 12403042). Y.Y.C. is grateful for funding for the training Program for talents in Xingdian, Yunnan Province (2081450001). X.L.Y. acknowledges the grant from the *National Nature Science Foundation of China* (No. 12303012), *Yunnan Fundamental Research Projects* (No. 202301AT070242). H.T.W. is supported by the Hebei Natural Science Foundation of China (No. A2022408002).

References

- Ajello, M., Greiner, J., Sato, G., et al. 2008, *ApJ*, 689, 666
Akylas, A., Georgakakis, A., Georgantopoulos, I., Brightman, M., & Nandra, K. 2012, *A&A*, 546, A98
Akylas, A., Georgantopoulos, I., Gandhi, P., Boorman, P., & Greenwell, C. L. 2024, *A&A*, 692, A250
Alexander, D. M., Bauer, F. E., Brandt, W. N., et al. 2003, *AJ*, 125, 383
Ananna, T. T., Treister, E., Urry, C. M., et al. 2019, *ApJ*, 871, 240
Andonie, C., Alexander, D. M., Rosario, D., et al. 2022, *MNRAS*, 517, 2577
Annun, A., Alexander, D. M., Gandhi, P., et al. 2025, *MNRAS*, 540, 3827
Antonucci, R. 1993, *ARA&A*, 31, 473
Assef, R. J., Stern, D., Kochanek, C. S., et al. 2013, *ApJ*, 772, 26
Bell, E. F., Papovich, C., Wolf, C., et al. 2005, *ApJ*, 625, 23
Boorman, P. G., Gandhi, P., Buchner, J., et al. 2025, *ApJ*, 978, 118
Boquien, M., Burgarella, D., Roehlly, Y., et al. 2019, *A&A*, 622, A103
Bower, R. G., Benson, A. J., Malbon, R., et al. 2006, *MNRAS*, 370, 645
Bruzual, G. & Charlot, S. 2003, *MNRAS*, 344, 1000
Buchner, J., Georgakakis, A., Nandra, K., et al. 2015, *ApJ*, 802, 89
Burlon, D., Ajello, M., Greiner, J., et al. 2011, *ApJ*, 728, 58
Calzetti, D., Armus, L., Bohlin, R. C., et al. 2000, *ApJ*, 533, 682
Carilli, C. L. & Walter, F. 2013, *ARA&A*, 51, 105
Carroll, C. M., Ananna, T. T., Hickox, R. C., et al. 2023, *ApJ*, 950, 127
Carroll, C. M., Hickox, R. C., Masini, A., et al. 2021, *ApJ*, 908, 185
Chabrier, G. 2003, *PASP*, 115, 763
Chang, Y.-Y., Le Floch, E., Juneau, S., et al. 2017, *ApJS*, 233, 19
Chen, C.-T. J., Hickox, R. C., Goulding, A. D., et al. 2017, *ApJ*, 837, 145
Churazov, E., Sunyaev, R., Revnivtsev, M., et al. 2007, *A&A*, 467, 529
Civano, F., Marchesi, S., Comastri, A., et al. 2016, *ApJ*, 819, 62
Comastri, A. 2004, *Compton Thick AGN: the dark side of the X-ray background* (Springer Netherlands), 245–272
Comastri, A., Gilli, R., Marconi, A., Risaliti, G., & Salvati, M. 2015, *A&A*, 574, L10
Dale, D. A., Helou, G., Magdis, G. E., et al. 2014, *ApJ*, 784, 83
Donley, J. L., Koekemoer, A. M., Brusa, M., et al. 2012, *ApJ*, 748, 142
Draine, B. T. & Li, A. 2007, *ApJ*, 657, 810
Elvis, M., Civano, F., Vignali, C., et al. 2009, *ApJS*, 184, 158
Esparza-Arredondo, D., González-Martín, O., Dultzin, D., et al. 2021, *A&A*, 651, A91
Esparza-Arredondo, D., González-Martín, O., Dultzin, D., et al. 2019, *ApJ*, 886, 125
Ferrarese, L. & Merritt, D. 2000, *ApJ*, 539, L9
Fiore, F., Puccetti, S., Brusa, M., et al. 2009, *ApJ*, 693, 447

- Fritz, J., Franceschini, A., & Hatziminaoglou, E. 2006, *MNRAS*, 366, 767
- Frontera, F., Orlandini, M., Landi, R., et al. 2007, *ApJ*, 666, 86
- Fruscione, A., McDowell, J. C., Allen, G. E., et al. 2006, in *Society of Photo-Optical Instrumentation Engineers (SPIE) Conference Series*, Vol. 6270, *Observatory Operations: Strategies, Processes, and Systems*, ed. D. R. Silva & R. E. Doxsey, 62701V
- Gao, F.-Y., Li, J.-Y., & Xue, Y.-Q. 2019, *Research in Astronomy and Astrophysics*, 19, 039
- Gehrels, N. 1986, *ApJ*, 303, 336
- Georgantopoulos, I. & Akylas, A. 2019, *A&A*, 621, A28
- Georgantopoulos, I., Pouliaxis, E., Ruiz, A., & Akylas, A. 2025, *A&A*, 695, A128
- Gilli, R., Comastri, A., & Hasinger, G. 2007, *A&A*, 463, 79
- Gilli, R., Norman, C., Calura, F., et al. 2022, *A&A*, 666, A17
- Goulding, A. D., Alexander, D. M., Bauer, F. E., et al. 2012, *ApJ*, 755, 5
- Guo, X., Gu, Q., Ding, N., Contini, E., & Chen, Y. 2020, *MNRAS*, 492, 1887
- Guo, X., Gu, Q., Ding, N., Yu, X., & Chen, Y. 2021, *ApJ*, 908, 169
- Guo, X., Gu, Q., Fang, G., et al. 2025, *A&A*, 694, A241
- Guo, X., Gu, Q., Xu, J., et al. 2023, *PASP*, 135, 014102
- Haardt, F. & Maraschi, L. 1991, *ApJ*, 380, L51
- Hickox, R. C. & Alexander, D. M. 2018, *ARA&A*, 56, 625
- Hopkins, P. F., Hernquist, L., Cox, T. J., et al. 2006, *ApJS*, 163, 1
- Kocevski, D. D., Brightman, M., Nandra, K., et al. 2015, *ApJ*, 814, 104
- Kormendy, J. & Ho, L. C. 2013, *ARA&A*, 51, 511
- Koss, M. J., Assef, R., Baloković, M., et al. 2016, *ApJ*, 825, 85
- Lacy, M., Petric, A. O., Sajina, A., et al. 2007, *AJ*, 133, 186
- Lacy, M., Ridgway, S. E., Gates, E. L., et al. 2013, *ApJS*, 208, 24
- Lacy, M., Storie-Lombardi, L. J., Sajina, A., et al. 2004, *ApJS*, 154, 166
- Laigle, C., McCracken, H. J., Ilbert, O., et al. 2016, *ApJS*, 224, 24
- Lambrides, E. L., Chiaberge, M., Heckman, T., et al. 2020, *ApJ*, 897, 160
- Lanzuisi, G., Civano, F., Marchesi, S., et al. 2018, *MNRAS*, 480, 2578
- Li, A. & Draine, B. T. 2001, *ApJ*, 554, 778
- Liang, E. P. T. 1979, *ApJ*, 234, 1105
- Luo, B., Brandt, W. N., Xue, Y. Q., et al. 2017, *ApJS*, 228, 2
- Lusso, E., Comastri, A., Vignali, C., et al. 2010, *A&A*, 512, A34
- Lyu, J., Alberts, S., Rieke, G. H., et al. 2024, *ApJ*, 966, 229
- Marchesi, S., Ajello, M., Marcotulli, L., et al. 2018, *ApJ*, 854, 49
- Marchesi, S., Civano, F., Elvis, M., et al. 2016, *ApJ*, 817, 34
- Masini, A., Civano, F., Comastri, A., et al. 2018, *ApJS*, 235, 17
- Mateos, S., Carrera, F. J., Alonso-Herrero, A., et al. 2015, *MNRAS*, 449, 1422
- Matt, G., Fabian, A. C., Guainazzi, M., et al. 2000, *MNRAS*, 318, 173
- Miyaji, T., Griffiths, R. E., & C-COSMOS Team. 2008, in *AAS/High Energy Astrophysics Division*, Vol. 10, *AAS/High Energy Astrophysics Division #10*, 4.01
- Moretti, A., Campana, S., Lazzati, D., & Tagliaferri, G. 2003, *ApJ*, 588, 696
- Mushotzky, R. F., Cowie, L. L., Barger, A. J., & Arnaud, K. A. 2000, *Nature*, 404, 459
- Netzer, H. 2015, *ARA&A*, 53, 365
- Padovani, P., Alexander, D. M., Assef, R. J., et al. 2017, *A&A Rev.*, 25, 2
- Planck Collaboration, Aghanim, N., Akrami, Y., et al. 2020, *A&A*, 641, A6
- Revnivtsev, M., Gilfanov, M., Sunyaev, R., Jahoda, K., & Markwardt, C. 2003, *A&A*, 411, 329
- Ricci, C., Bauer, F. E., Treister, E., et al. 2017a, *MNRAS*, 468, 1273
- Ricci, C., Trakhtenbrot, B., Koss, M. J., et al. 2017b, *ApJS*, 233, 17
- Ricci, C., Ueda, Y., Koss, M. J., et al. 2015, *ApJ*, 815, L13
- Richstone, D. O. & Schmidt, M. 1980, *ApJ*, 235, 361
- Scoville, N., Aussel, H., Brusa, M., et al. 2007, *ApJS*, 172, 1
- Steffen, A. T., Strateva, I., Brandt, W. N., et al. 2006, *AJ*, 131, 2826
- Stern, D. 2015, *ApJ*, 807, 129
- Torres-Albà, N., Marchesi, S., Zhao, X., et al. 2021, *ApJ*, 922, 252
- Treister, E., Urry, C. M., & Virani, S. 2009, *ApJ*, 696, 110
- Ueda, Y., Akiyama, M., Hasinger, G., Miyaji, T., & Watson, M. G. 2014, *ApJ*, 786, 104
- Urry, C. M. & Padovani, P. 1995, *PASP*, 107, 803
- Weaver, J. R., Kauffmann, O. B., Ilbert, O., et al. 2022, *ApJS*, 258, 11
- Xue, Y. Q. 2017, *New A Rev.*, 79, 59
- Zhang, R., Guo, X., Gu, Q., et al. 2025, *ApJ*, 987, 46

Appendix A: Parameters of MIR-selected AGNs

This section presents a tabular summary of the MIR-selected AGN sample used in this study, the relevant parameters, and the identified CT-AGNs.

Table A.1: Parameters adopted for CT-AGN selection from the MIR-selected AGN sample and summary of the identified CT-AGNs.

ID	R.A. ($^{\circ}$)	Decl. ($^{\circ}$)	z	$B_{3''}$	T_{exp} (ks)	$f_{2-10}^{\text{up-limit}}$ ($10^{-16} \text{ erg cm}^{-2} \text{ s}^{-1}$)	$\log L_{2-10}$ (erg s^{-1})	$\log \nu L_{\nu}(6 \mu\text{m})$ (erg s^{-1})	α_{AGN}	$\log M_{\star}$ (M_{\odot})	$\log \text{SFR}$ ($M_{\odot} \text{ yr}^{-1}$)	CT flag
(1)	(2)	(3)	(4)	(5)	(6)	(7)	(8)	(9)	(10)	(11)	(12)	(13)
571	149.6744	1.6249	0.76	3	88.30	44.23	42.947	42.864	1.000	8.822	0.171	0
2050	149.6823	2.2929	1.99	7	183.52	32.07	43.698	43.820	0.773	10.135	0.746	0
3175	149.8748	2.6273	1.99	8	181.39	35.00	43.735	43.721	1.000	9.897	0.940	0
4623	150.3852	1.7087	1.48	5	190.98	25.80	43.340	43.241	1.000	9.252	0.729	0
61366	150.2570	2.2118	1.75	0	189.12	10.90	43.117	45.571	1.000	10.927	1.788	1
69254	150.5989	2.1318	1.10	4	193.94	22.83	43.010	43.596	1.000	9.214	0.103	0
69426	150.4179	2.2177	0.57	2	182.79	18.35	42.294	43.825	1.000	10.605	0.727	1
70003	150.6131	2.4660	1.98	6	219.78	24.63	43.578	43.681	0.864	9.773	1.110	0
106842	150.6229	1.9051	1.67	3	231.31	16.89	43.264	43.790	1.000	8.477	0.068	0
107028	150.3769	2.7157	0.94	6	190.92	28.35	42.952	44.980	1.000	10.897	1.974	1
109199	150.1546	2.8030	0.60	1	91.08	30.27	42.554	43.291	1.000	10.054	1.049	0
133669	149.8801	2.3016	1.95	6	209.43	25.85	43.585	43.988	1.000	10.028	0.942	0
134768	149.5189	2.3015	1.41	7	69.26	84.98	43.810	43.595	0.999	9.986	1.278	0
135400	149.8988	1.8028	1.92	11	192.42	39.97	43.763	43.779	1.000	9.760	1.165	0
136577	150.3656	2.3868	1.93	8	215.15	29.51	43.635	43.813	1.000	9.340	1.300	0
⋮	⋮	⋮	⋮	⋮	⋮	⋮	⋮	⋮	⋮	⋮	⋮	⋮
898638	149.4213	2.0407	1.48	1	44.37	62.13	43.717	45.127	1.000	10.606	1.862	0
899015	149.6794	2.2080	1.02	6	186.81	28.98	43.044	44.834	1.000	10.461	2.242	1
899719	150.4337	2.7086	2.00	4	191.12	23.16	43.559	44.042	1.000	9.131	0.139	0
927043	150.5996	2.0402	1.20	5	159.05	30.98	43.227	43.546	1.000	8.527	-0.310	0
927564	150.1823	1.7008	0.72	4	185.35	23.89	42.625	44.780	1.000	10.617	1.410	1
927986	150.5286	2.8744	1.51	2	111.99	29.96	43.423	43.747	1.000	9.103	-0.263	0
932400	150.5801	2.8731	0.79	2	103.83	32.31	42.855	42.805	1.000	8.421	0.188	0
932754	150.3066	2.1149	0.41	13	235.73	36.30	42.285	43.790	1.000	10.678	0.527	1
933121	150.5423	2.0232	1.62	4	183.94	24.07	43.390	43.421	1.000	10.037	0.708	0
946717	150.1100	1.9535	0.54	7	213.00	27.63	42.425	43.978	1.000	10.675	1.454	1
964368	150.1913	1.7899	0.70	8	188.73	33.64	42.747	43.747	1.000	10.276	0.752	0

Notes. This table is available in its entirety in the machine-readable format. Only a portion of this table is shown here to demonstrate its form and content. Col. (1) contains IDs from the COSMOS2020 FARMER catalog. Cols. (2) and (3) contain the R.A. and decl. of the sources. Col. (4) contains the photometric redshift that we used. Col. (5) is the background counts of the source within a radius of $3''$. Col. (6) represents the exposure time at the source location. Col. (7) contains the upper limit of 2–10 keV flux density. Col. (8) contains the logarithm of 2–10 keV luminosity upper limit in the rest-frame. Col. (9) contains the logarithm of $6 \mu\text{m}$ luminosity for an AGN in the rest-frame. Col. (10) contains the confidence of AGN components for SED fitting. Cols. (11)–(12) contain the logarithm of M_{\star} , and SFR for AGN host galaxy. Cols. (13): CT-AGN flag; "1" = CT-AGN identified in this work.